

# Contents lists available at ScienceDirect

# Materialia

journal homepage: www.elsevier.com/locate/mtla



# Molecular dynamics simulation of stress induced by energetic particle bombardment in Mo thin films



Meng Zhang a,b,\*, Zhaoxia Rao b, Kyung-Suk Kim b, Yue Qi b, Liang Fang a,c, Kun Sun a, Eric Chason b

- <sup>a</sup> State Key Laboratory for Mechanical Behavior of Materials, Xi'an Jiaotong University, Xi'an 710049, PR China
- <sup>b</sup> School of Engineering, Brown University, Providence 02912, USA
- c School of Mechanical & Electrical Engineering, Xiamen University Tan Kah Kee College, Zhangzhou 363105, PR China

#### ARTICLE INFO

# Keywords: Molecular dynamics simulation Sputter deposition Stress evolution Kinetic model Defects evolution

#### ABSTRACT

Molecular dynamics (MD) simulations are performed to analyze the evolution of defects and stress caused by low-energy (25-400 eV) Ar bombardment of polycrystalline Mo thin films. Simulations were performed under different conditions to explore the role of grain boundaries (GBs), Ar-atom's kinetic energies, and incident directions on defect generation. The results show that the GBs enhance the production of interstitial defects, producing compressive stress at much larger depths than the implantation range. This is attributed to sequences of atomic collisions that knock atoms into GBs instead of a diffusional process. Decreasing the grain size or increasing the kinetic energy of the incoming particles increases the number of interstitials in the film, which increases the compressive stress. The incident angle has little influence on the number of interstitials in the film, but the sputtering yield depends on the polar angle. The stress distribution can be modeled by a superposition of the different defect distributions with the appropriate relaxation volumes.

# 1. Introduction

Low energy particle bombardment plays an important role in many materials processing techniques such as sputter deposition, ion-assisted growth, depth profiling, etching, implantation, and micromachining. In many cases, stresses produced during processing can be large enough to affect performance and impact reliability. Energetic particles can have a significant effect on the stress, e.g., in the use of ion-assisted [1] or sputter deposition [2] to modify film stress or ion bombardment to tailor the stress distribution in micromachined devices [3]. Therefore, it would be useful to have a deeper understanding of how they affect the stress in order to predict it and optimize processing conditions.

Studying the relationship between energetic particle bombardment and stress generation has a long history. Early models attributed the stress modification as being analogous to "atomic peening" [4, 5] in which momentum transfer from the energetic particle drives the atoms in the film into more dense configurations [6] or creates stress-inducing defects. Other models have been proposed [2, 5, 7–14] that use the generation and trapping of defects to explain the contribution of energetic particles to the stress. These processes may occur in the bulk of the film, but it has also been recognized that GBs can play a role in modifying the stress-generation processes [14–17]. Samaras et al. [18] found that GBs

act as sinks for interstitials by using MD simulation for face-centered cubic (FCC) Ni and body-centered cubic (BCC) Fe. The efficiency of "defect absorbency" strongly depends on the GB characters [19]. For instance,  $\Sigma$ 29 twist GBs in Fe has stronger interstitial absorbency, which leaves an excess concentration of vacancies in the bulk region [20]. The absorbed interstitials can lead to increasing generation of stacking-fault tetrahedral in Ni [21] or even result in GB migration [22, 23]. When displacement cascades are near to or overlap with a GB plane, the GB structure may be changed, e.g., becoming curved [24], increasing in width or generating stress-concentration near GB [25].

Despite many studies, many of the fundamental mechanisms are not well understood. For instance, the role of trapped neutral atoms in creating stress has been proposed [17]. Based on the knock-on linear cascade theory [26], Windischmann [7] pointed out that the rate per unit area with which atoms are displaced from equilibrium sites is proportional to the energy and ion flux. A simple model was proposed by Davis [10], which describes the formation of steady-state stress in the film by coupling the stress generated by knock-on implantation of film atoms and stress relaxation excited by thermal spike. However, other works suggest that the stress is not related to the number of trapped atoms but associated with parameters such as the modulus of elasticity, Poisson ratio, and net deflection of the wafers in the orthogonal directions  $\boldsymbol{x}$  and  $\boldsymbol{y}$ 

<sup>\*</sup> Corresponding author at: State Key Laboratory for Mechanical Behavior of Materials, Xi'an Jiaotong University, Xi'an 710049, PR China. E-mail address: mengzh@stu.xjtu.edu.cn (M. Zhang).

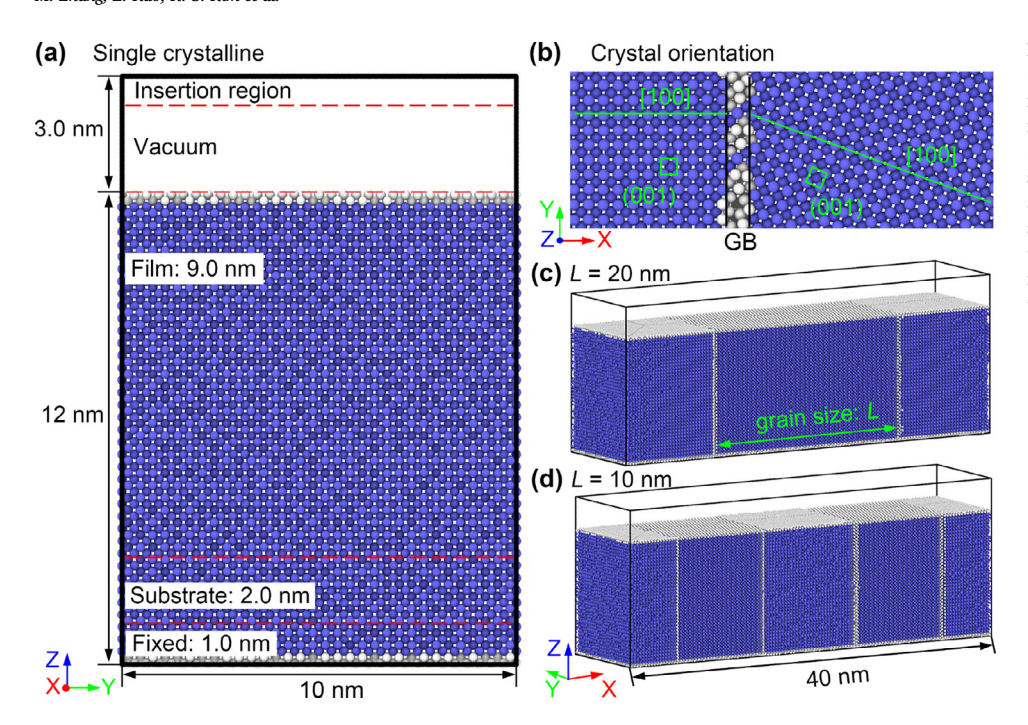


**Fig. 1.** (a) Relaxed single crystalline model. (b) Crystal orientation of adjacent grains after relaxing, where the white atoms on surface are removed for clarifying the orientation. (c) and (d) Relaxed polycrystalline model with grain size of 20 nm and 10 nm, respectively. The blue and white atoms represent BCC and unknown structures, respectively (For interpretation of the references to color in this figure legend, the reader is referred to the web version of this article.).

[27]. A further model [14] suggested that the stress can be calculated from a few parameters of the grains (e.g., the total lateral dimension of one grain and the mean thickness of the inter-crystalline zone) and that the point defects can escape from the film, annihilate with each other, or be absorbed in the dislocation or GBs. Although these models can describe the relationship of defects and stress, they do not give any microscopic information on the type of defects responsible for the stress, as well as the respective role of the interstitials, vacancies, substitutional of recoil atoms [28].

To further our understanding, this work describes the use of molecular dynamics simulation to characterize the defects and stress induced by energetic Ar bombardment of Mo films. Previous studies have also used MD simulation to model the effects of low energy particle bombardment, e.g., densification, [6] defect formation [29, 30] film growth modification [31—37]. The focus of the current work is on characterizing the fundamental mechanisms by which the stress is created during particle bombardment. Simulations were performed on films with different grain sizes to explore how the defect production is modified in the presence of GBs. The resulting stress distribution was modeled by a superposition of defect distributions with different relaxed volumes.

The stress distribution was used to estimate the residual stress in growing films induced by defect production. Since the time scale of MD simulations is short, the work only reveals the ballistic processes that occur at a short time and does not consider potential relaxation of the stress mediated by long-range diffusion of the particle-induced defects. In many systems, the stress depends on the growth rate [38, 39], which suggests that the post-implantation dynamics of the particle-induced defects are important, not just the stress that is generated by atomic collisions. To consider defect kinetics, the results from the work here can be used as input for other computational methods such as kinetic Monte Carlo [40–42] or rate equations [43].

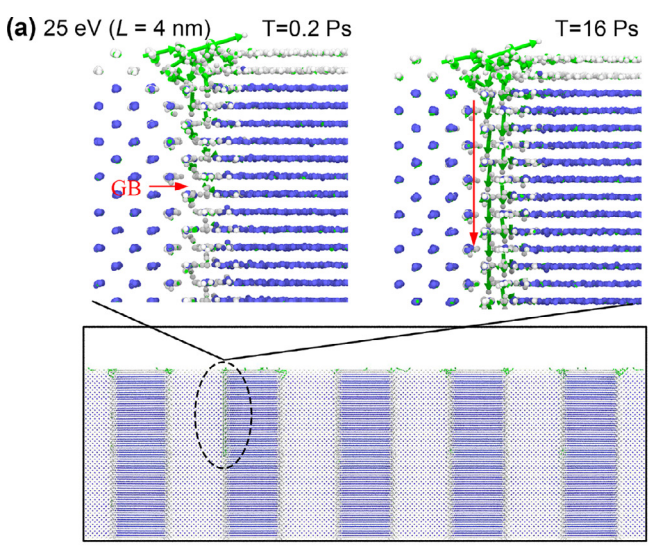
# 2. Simulation method

A schematic of the simulated geometry is shown in Fig. 1. The total volume is the same for all of the simulations with dimensions of 40 nm  $\times$  10 nm  $\times$  15 nm ( $x \times y \times z$ ). The initial crystal height is 12 nm, so the total number of Mo atoms is approximately 310,000. Periodic boundary conditions were used along the x- and y-directions, while the z-direction was kept free. Fig. 1a corresponds to a plan view of a sin-

gle crystalline BCC Mo film with its <100> axes parallel to the coordinate system. Fig. 2b–d correspond to the crystal orientation of adjacent and polycrystalline films with GBs inserted in the crystal at spacings of L=20 and 10 nm. The GBs were generated by alternately rotating each region by 20° around the z-axis (<001>). Thus, all grain boundaries are symmetric tilt GBs, which are close to the  $\sum 13a(22.6°[100])$  GB. This type of GB has large boundary energy [44] and a large influence on the range of defect absorption [45]. The two end grains are the same, from the periodic boundary conditions, so that there is no GB between them. All the GBs are taken to be normal to surface, although this geometry varies from the real system, it still provides a means to investigate the mechanisms that control stress evolution in thin films.

All structures were initially relaxed at 300 K and 0 GPa for 200 ps in isothermal-isobaric (NPT), which allows the configurations at the GBs to relax. After that, the Mo atoms in the three regions shown in Fig. 1a were relaxed for an additional time of 200 ps, i.e., the top 9 nm of Mo atoms corresponds to the film and uses a microcanonical (NVE) ensemble, the next 2 nm corresponds to the substrate and uses a canonical (NVT) ensemble at 300 K, the bottom 1 nm corresponds to a fixed region and used fixed conditions. The time step for all the simulations was set to be 0.002 ps. In the insertion region, Ar atoms were introduced into the simulation along the negative z-direction with recoil energy  $(E_k)$ . Different simulations corresponding to energies of 25-400 eV were performed. The total number of incoming Ar atoms was 1200 for each set of conditions studied. In each cycle, the system was relaxed after a new Ar atom was introduced from the insertion region, as shown in Fig. 1, which contains two steps: (1) a 20 ps simulation was run in the NVE ensemble for the 9 nm film and Ar, which is enough to model the interaction between Ar and Mo film. (2) then NVT ensemble is simulated for a time of 12 ps at 300 K to make the incoming Ar and Mo film relax and maintain the temperature at a pre-defined value. The time in step (1) is sufficient to capture all the displacements and defect formation associated with a single energetic Ar particle. However, it is too short to simulate any long-range diffusional processes that occur afterward. Steps (1) and (2) are repeated until the number of incoming Ar reaches 1200.

All simulations were performed utilizing the LAMMPS software package [46] at a temperature of T = 300 K. Three kinds of potentials were used in this simulation: Lennard-Jones (LJ) 6-12 potential, [47] ZBL po-



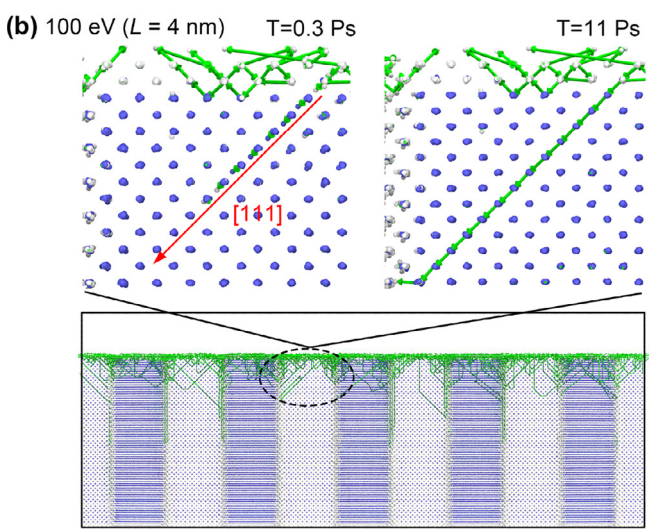


**Fig. 2.** Interstitial generation at low energy (a) and high energy (b). Atoms are colored according to the CNA: BCC (blue) and unknown (white) structure. The green arrows pointed from initial to final position of atoms are displacement vectors (For interpretation of the references to color in this figure legend, the reader is referred to the web version of this article.).

tential, [48] and embedded atom method (EAM) interatomic potential [49]. The LJ potential was chosen to describe interaction between Ar atoms with parameters  $\sigma=3.405$  Å and  $\varepsilon=0.0104$  eV [50]. The ZBL potential describes the short-range and high-energy collision between Ar and Mo atoms. The cutoff distance  $(r_c)$  of ZBL potential is 2.225 Å calculated by using  $r_c=\sqrt{2}a_0/2$  [51, 52], where  $a_0$  is the lattice constant of Mo that is equal to 3.1472 Å. The high-energy interatomic interactions occur at short distances, typically up to 1 Å [53]. Thus, the ZBL potential with the cutoff of  $r_c$  can well describe the high energy collision between Ar and Mo atoms. Finally, the EAM potential proposed by Ackland and Thetford [49] was used to describe the interaction of Mo-Mo atoms.

The OVITO software [54] was used to identify and visualize the crystal structures via the common neighbor analysis (CNA) technique. The dislocations are detected by using the Dislocation Extraction Algorithm (DXA) [55]. The Wigner-Seitz cell [56] and the Voronoi-cell [57] are used to find and count different defects in the periodic crystalline and GBs structures, respectively. If there are two (or more) atoms in a same cell, there are one or more interstitials, and an empty cell corresponds to a vacancy. The Voronoi-cell can be constructed by drawing the perpendicular planes at the midpoint of two neighbor atoms. Thus, the shapes

**Table 1**Comparison of threshold displacement energies at different directions between MD calculations and experiments, where the experimental values are taken from Ref. [62] at 8 K, Ref. [61] at 70—150 K.

Direction	MD, $E_d^l$ (eV)	Exp., (eV)	Exp., (eV)
<100> <110> <111> <112>	32 62 36 46	$35^{+1}_{-2}$ [62] > $2E_{d<100>}$ [62] $45\pm3$ [62]	34.5±0.5 [61]

of the cell are determined by the neighboring atoms, e.g., tetradecahedron for a perfect BCC atom and polyhedron for the disordered atom (in surface or GBs). The stress for each atom is calculated in the MD simulation using a method described in Refs. [36, 58, 59]; further detail is provided in the supplementary material.

#### 3. Results and discussion

Simulations were performed at a range of energies (25–400 eV), grain sizes (single crystal and L=4, 5, 6.67, 10, and 20 nm), and bombardment directions ([001], [011], [111], [112], and different polar angles). The resulting defect distribution and corresponding stress were characterized. The energy range was chosen because it is relevant for numerous processes, e.g., sputter deposition, ion-assisted deposition, and depth profiling. Only the effects of energetic Ar bombardment are reported here. Although deposited Mo atoms can have similar energies to Ar during sputter deposition, generally there are no Mo atoms at higher energies.

# 3.1. Generation of defects in polycrystalline thin film

Generally, the displacement process in the bulk depends on the relationship between recoil energy and threshold displacement energy (TDE,  $E_d$ ). When the recoil energy is above the minimum  $E_d^l$  where the value is determined by the temperature, direction of recoil atom, and strain, a stable displacement occurs [60]. However, in such case, the defects may not survive due to recombination as the thermal spike anneals. The value of  $E_d$  at 300 K obtained from 25 independent simulations for directions of <100>, <110>, <111>, and <112> are tabulated in Table 1. The simulation and calculation method can be seen in the supplementary material. The values from MD reports are in good agreement with the experimental data, but are slightly smaller than that from experimental data, which is caused by the high temperature in this simulation [61].

GBs, investigated by previous experiments [63, 64] and computer simulations [65], are considered to be non-equilibrium structure that lack both short- and long-range order. It may not be so anomalous [66], but there are many disordered atoms, which leads to high surface energy and free volume in GBs [67]. The interstitials prefer the free volume, and the adatoms can further reduce the Gibbs free energy of GBs [68].

The role that GBs play in interstitial generation can be understood by looking more closely at the process on the atomic scale. Fig. 2 shows the displacement vectors of the atoms after Ar collisions for (a) 25 eV and (b) 100 eV. At the higher energy, displacements of atoms in the bulk lead to a sequence of collisions along close-packed rows that end up with the formation of interstitials in the GBs. This mechanism has been pointed out previously by Silsbee [69], who referred to it as focusing. It enables interstitials to be created at much larger distances from the knock-on atom than just the amount it is displaced. When GBs are present, they can act as traps for interstitials that reduce the recombination of and annihilation of the interstitial defects with vacancies or the free surface. Hence, many more interstitials are formed in the GB at a greater depth than would be formed in a single crystal for the same Ar energy.

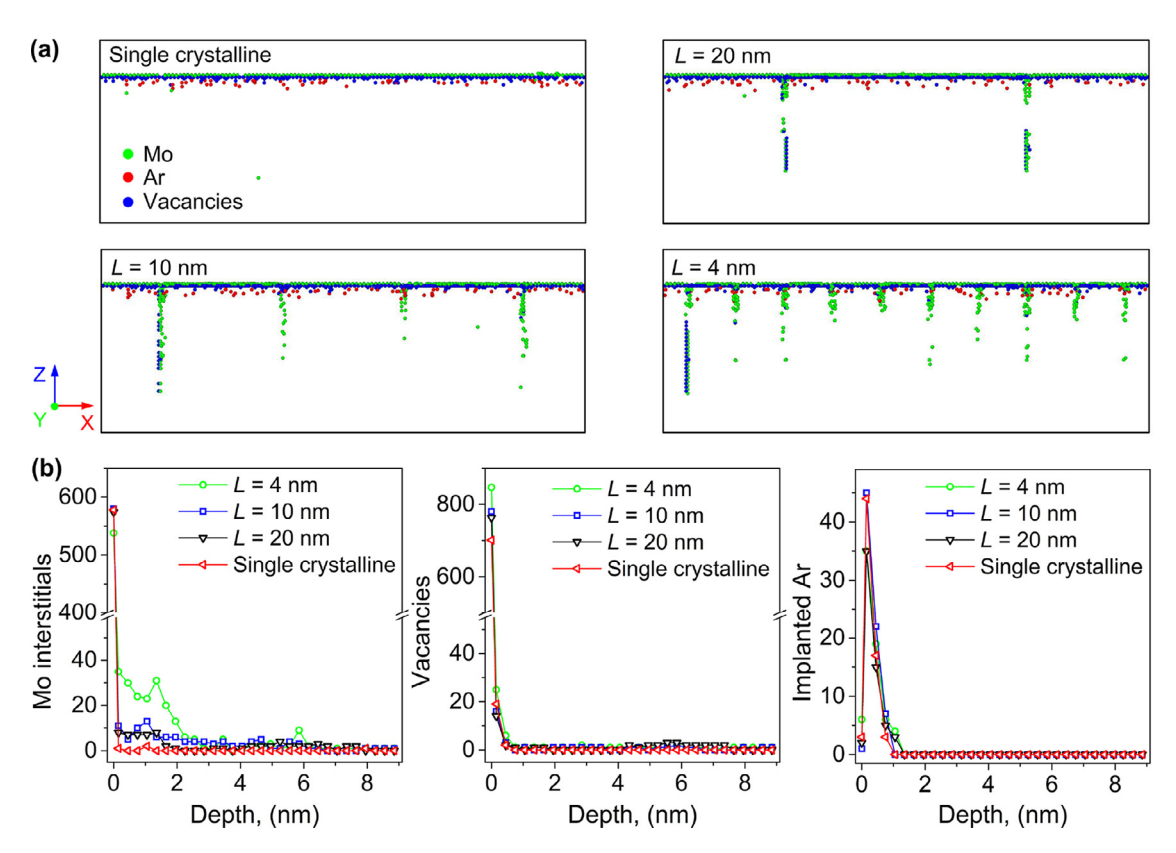


Fig. 3. (a) Distribution of displaced Mo atoms, vacancies and implanted Ar after 1,200 Ar collisions at 100 eV, where the green, red, and blue atoms represent Mo, Ar, and vacancies, respectively. (b) Depth distribution of defects for different grain sizes at 100 eV (For interpretation of the references to color in this figure legend, the reader is referred to the web version of this article.).

However, the process is slightly different at the lower energy, as can be seen from Fig. 2a. The displacement vectors indicate that the formation of GB interstitials is due primarily to sequential collisions occurring within the GB, not from displacements that originate in the bulk. The low crystalline symmetry of atoms in the GBs results in the lower binding energy of atoms than those in the bulk, which makes the displacement of the atom along the boundaries easier.

# 3.2. Defects at different grain sizes, energies, and bombardment directions

## 3.2.1. Grain sizes

This section discusses the defect distribution produced by Ar bombardment on Mo films with different numbers of GBs in the recoil direction of [001]. An example showing the spatial distribution of defects generated by 100 eV Ar, averaged over the *y*-direction, is shown in Fig. 3a. The images correspond to the morphology after 1200 Ar atoms, and the four panels correspond to different grain sizes indicated in the figure. Displaced Mo atoms are shown in green; they go into interstitial sites in the lattice or at the GBs. The corresponding vacancies are shown in blue. At 100 eV, approximately 70% of the implanted Ar atoms (red) reside in interstitials sites, with the remainder on substitutional sites. When the energy is raised to 400 eV, the number of Ar on interstitial sites is approximately equal to the number on substitutional sites.

The depth distribution of the different defects, averaged over the *x*-and *y*-dimensions, is shown in Fig. 3b for the different simulated grain sizes. For the single crystalline model (no GBs), most of the defects at 100 eV form in the first nm below the surface. Similarly, such behavior occurs at the energies of 25 eV and 50 eV. The Small recoil energy makes it difficult to displace atoms in the bulk, but it can lead to the movement of atoms along GBs due to their low crystalline symmetry. The depth distributions of the vacancies and the implanted Ar do not change significantly when the grain size is changed. However, the ad-

dition of GBs significantly modifies the depth distribution for the interstitials since the defects were generated by sequential collision within boundaries at low energy. When the grain size is decreased, a larger number of interstitial defects are created at larger depths. The spatial distribution in Fig. 3a shows that this is due to a large number of interstitial defects that form along the GBs. Away from the GBs, in the center of the grain, the distribution of interstitials is unchanged.

# 3.2.2. Energies

Simulations were also performed for different energies at different grain sizes. The spatial distribution of defects in a film with L=4 nm at different Ar energies are shown in Fig. 4a. At the low energy (25 eV and 50 eV), there are few defects that distribute in the bulk since the energy of primary knock-on atom (PKA) obtained from the Ar is less than the  $E_{d[100]}$ . However, the defects distribution in the vicinity of the GBs is dense, especially at 50 eV. Based on this phenomenon, it can be concluded that GBs in thin films provide more energetically favorable sites, which can significantly block the recombination between interstitials and vacancies in the quenching stage. At 400 eV, some of the defects are created at depths beyond the simulation size, but simulations with a larger Mo film thickness confirm that this does not change the defect or stress distribution inside the simulated region.

The number of defects of all types increases as the energy is increased from 25 eV to 400 eV. The depth at which the defects are formed also increases with energy. Importantly, as the energy increases, there is an increasing tendency to create interstitials in the GBs. Depending on the energy, there are 3-6 times more interstitials formed in the region within +/-0.6 nm of the GBs than in the rest of the film. The GBs interstitials are also created at a larger depth than those in the bulk of the film

In addition to point defects, by using the DXA, we also found that there are one or two small interstitial prismatic-dislocation loops with a

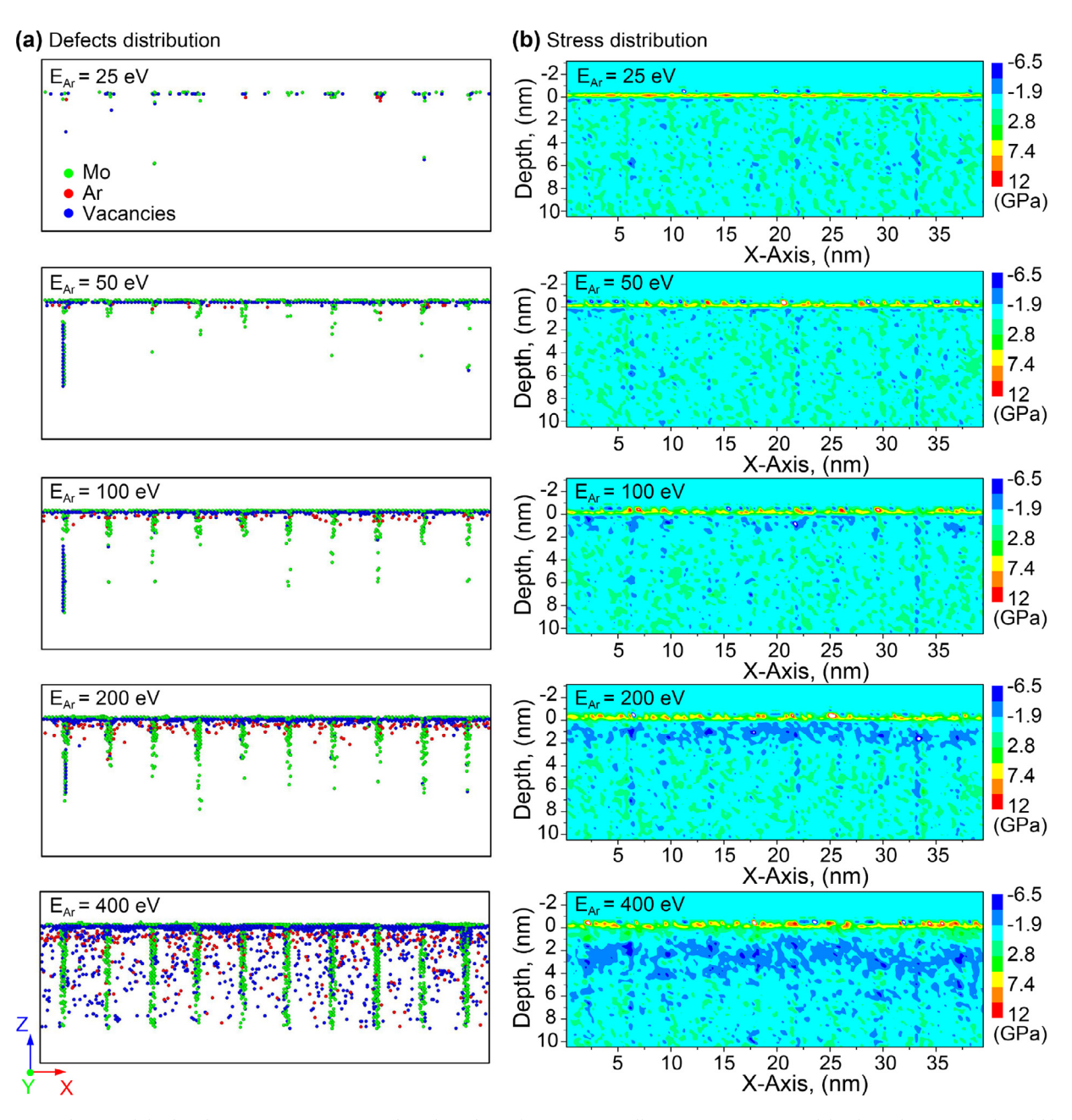


**Fig. 4.** (a) Distribution of displaced Mo atoms, vacancies and implanted Ar after 1,200 Ar collisions in L = 4 nm model, where the green, red, and blue atoms represent Mo, Ar, and vacancies, respectively. (b) Stress distribution in L = 4 nm after 1,200 collisions at different energies (For interpretation of the references to color in this figure legend, the reader is referred to the web version of this article.).

diameter approximate 5-7 Å after 1,200 collisions in single crystalline and L=20 nm. Vacancy loops were not found because the formation of such a loop is associated with the collapse of a vacancy-rich core, which is generated by high energy-density deposition in Mo [70]. The interstitial loops are typically formed for the ion energy  $\geq 300$  eV. Most of the loops have Burgers vectors  $\mathbf{b}=\mathbf{a}<100>$ , which agrees well with the experimental study of ion bombardment on (001) Mo foil [71]. The large energy results in many interstitials generated in the bulk in the two models. However, with the decrease of grain size, most interstitials are captured by GBs instead of clustering, as can be seen in the defect distribution in Fig. 4a. For the L=10 nm model, the dislocation loop is not found, indicating that there are no large interstitial clusters after 1,200 collisions. According to the research [45], the influence range of interstitial absorption for  $\sum 13a(22.6°[100])$  in Mo is about 1.65 nm. The interstitials can migrate into the GB with a low barrier when they

are within this range. Therefore, in the model with a grain size smaller than 10 nm, it is difficult to generate large interstitial clusters in the bulk region since interstitials can migrate into GBs easily.

Sputtering yield,  $Y_s$ , is a very important parameter that is used to describe the sputtering process quantitatively, which is defined as the mean number of atoms sputtered (removed) per incident ion [51]. The sputtered atoms will be obtained enough energy to overcome the surface binding energy and move away from the surface. Therefore, the  $Y_s$  at different energies are also calculated, and a comparison with the theoretical model and experimental data is carried out. The model proposed by Bohdansky [72] is used to calculate the  $Y_s$ , which includes a correction factor to Sigmund's model [73] for better correlation with published experimental results of sputtering yields. The detailed information of the model and some parameters for Mo film in the model can be seen in supplementary materials.

**Table 2**Total number of defects in film and sputtering yield at different recoil directions.

	[001]	[011]	[111]	[112]	10°	20°	30°	40°
Mo Interstitials	744	663	555	672	727	733	768	698
Vacancies	940	1033	1038	1107	963	998	1111	1114
Interstitials Ar	59	12	9	48	54	53	56	26
Substitutional Ar	17	8	6	6	19	19	8	11
Sputtering yield, $Y_s$	0.148	0.293	0.378	0.349	0.17	0.217	0.268	0.312

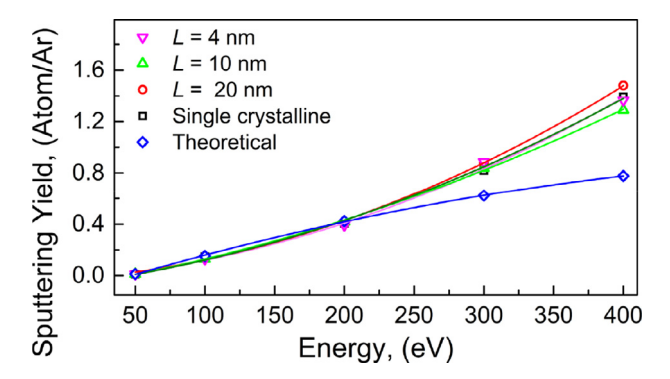


Fig. 5. Sputtering yield of Mo surface bombarded by Ar atoms at varying energies.

Fig. 5 shows the variation of Y<sub>s</sub> after 1,200 collisions and calculated Y<sub>s</sub> for the four models at different energies and normal incidence angle. It is significant that these values are in good agreement with theoretical results at low energies. The average value for MD simulation at 50 eV, 100 eV, and 200 eV, respectively, are 0.011, 0.138, and 0.4, which are also consistent with the values obtained by in situ weight-loss measurements in Ref. [74]. However, at 400 eV, the  $Y_s$  is slightly larger than the theoretical value. Two reasons are considered for this phenomenon. The first is that some surface atoms penetrate across the entire bulk through the channeling when they obtain large energy from Ar. It is hard to subtract the number of such atoms since counting these atoms is difficult during the 1,200 collisions. Secondly, at high energy, the damage in the surface region is serious, as can be seen by the vacancies on surface (blue spheres) in Fig. 4a. Therefore, the atomic symmetry in the collision region becomes lower than before, which leads to the decrease of binding energy for surface atom. When the next Ar bombard in the vicinity of the region, it is easy to make the surface atom reflect from the surface.

# 3.2.3. Bombardment directions

Similarly, some typical directions, i.e., [001], [011], [111], and [112] and random directions with polar angles of 10, 20, 30, and 40 degrees are selected for Ar bombarding on (001) surface in L = 5 nm model at 100 eV. After 1200 collision, the number of defects at different directions are summarized in Table 2. It can be found that the  $Y_s$  at [001] direction and 10 degree for the model are consistent with the above theoretical results and experimental values [74]. The value increases with improving polar angle, which is in good agreement with the researches [51, 75]. Such behavior can be attributed to two reasons, i.e., deposition profile and  $E_d$ . With the impact angle increase, the deposition profile is shifted closer to the surface, which leads to a yield enhancement [75]. It is interesting that the polar angle of [011] is larger than that of [112] directions, but the yield shows the opposite trend. This behavior may be associated with the  $E_d$  [76], as shown in figure S1 of supplementary materials. To destroy the sub-surface structure (two or three top layer atoms), it needs large energy of PKA in [011] direction. As a result, some sputtered atoms return to the surface at the energy of 100 eV for this direction.

The depth distribution of different defects, averaged over the x- and *y*-dimensions, is shown in Fig. 6 for the energy of 100 eV and L = 5 nm. Although the difference of  $E_d$  between these directions is larger, especially for the [011] direction, which is approximately twice than that in [001] direction at 300 K, the depth distribution of the interstitials and vacancies do not change significantly. The main reason is that most of collisions between Ar and PKA of Mo are not head-on collision. Thus, the majority of PKA collisions will not be along the same direction as incident Ar. In addition, the collision region will overlap with the grain boundaries at different directions in L = 5 nm model, which leads to defects being absorbed by GBs easily. Therefore, the effect of PKA's direction on defects is reduced in the model with a small grain size. For the Ar defects, the implanted depths are similar in these directions. However, the number of implanted Ar is associated with the polar angles. At the same surface binding energy of (001) surface, the projectile Ar can directly implanted into the film at <001> direction instead of undergoing back-reflection. The  $E_d$  for [001] direction is also smaller than that of other directions, which makes Ar implant into and retain in the film

Since the simulations are performed at room temperature and a short time scale, the diffusion distance of interstitials in the Mo film is very small. Hence, the incorporation of additional atoms into the GB is primarily generated by direct collisions that allow adatoms to incorporate into more energetically favorable sites, and long-range diffusion-mediated processes do not play a significant role. The diffusion-less defect generation at GBs is consistent with the mechanism proposed by Chason *et al.* [17] in their analytical model of stress in sputter-deposited films, as discussed in more detail below.

Fig. 3 and 4 indicate that there are some configurations of interstitial/vacancy pairs produced deep in the GB. These appear in the figure as short line segments of blue and green defects in the GB. The production of these was explored by looking at the sequence of short-range diffusion leading to their formation. In these cases, an annihilation region overlaps with the GB when a collision occurs in the vicinity of the GB. During the annihilation process, the defects near or within the GB will diffuse into the annihilation region and recombine the defects located at the GB. From the research [45], the diffusion barrier for different types of GBs in BCC metals is very low when the defects are in the GB's influence region. For instance, the average barrier of vacancy annihilation is 0.24 at the influence range of 1.25 nm and a temperature of 93 K for Mo. Thus, at the temperature of 300 K, the interstitial/vacancy can spontaneously recombine within the influence region. When the interstitials diffuse into a GB, some atoms located in adjacent layer below will be dragged/pushed into the GB and become the GB's atom. Then this process continues due to the low diffusion barrier until an array of vacancy/interstitial defect pairs is produced along a segment of the GB. The process can be seen in more detail in figure S2 of the Supplementary material (Image of the process for vacancy/interstitial defects produced deep in the GB). Because an atom is displaced from GB to adjacent grain, the formation of these Frenkel pairs is also accompanied by GB migration. This migration induced by irradiation and diffusion is also observed in experimental and simulation in Cu [23]. For defects that are produced next to each other, they would likely recombine if the time scale of the simulation was long enough for defect diffusion to occur.

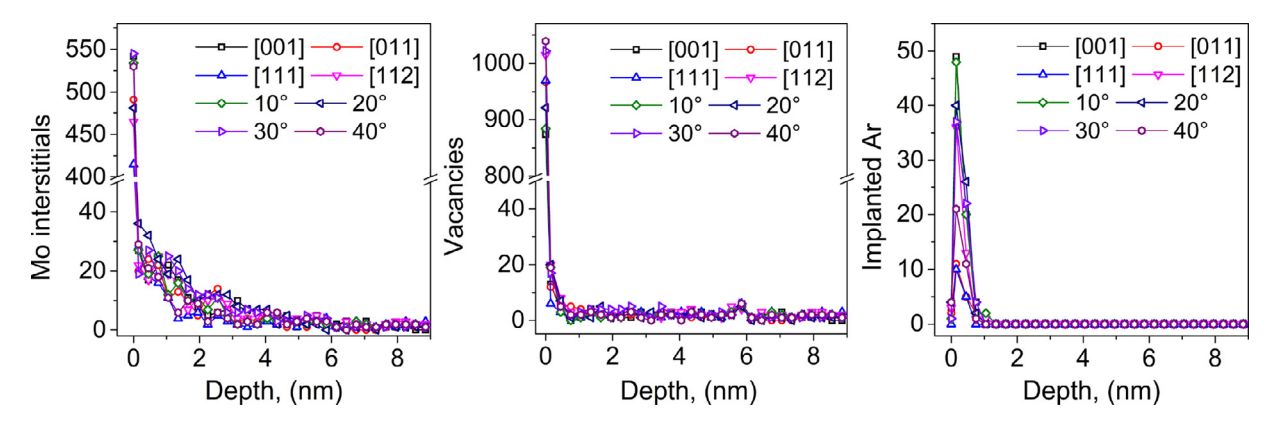


**Fig. 6.** Depth distribution of defects for different incident directions at 100 eV for L = 5 nm.

# 3.3. Stresses for different grain sizes, energies, and bombardment directions

The corresponding stress was also calculated for the simulations at different grain sizes, energies, and bombardment directions. The spatial distribution of stress within the film for L = 4 nm at different energies is shown in Fig. 4b after the introduction of 1200 Ar particles. The images show that there is a highly tensile region near the surface. Much of this is present after relaxation, even before any energetic particles are introduced. Therefore, this can be attributed primarily to the surface stress that is generated by a large number of broken bonds on the thin film surface [77]. After particle bombardment is performed, additional tensile stress is generated in the near-surface region due to vacancies created there. Below this region, a compressive band of stress forms due to the interstitials and implanted Ar. At higher energies, the compressive stress region forms at greater depths in the film, correlated with the change in the distribution of defects. The stress is fairly uniform across the lateral x-direction in the film, even though there are more interstitial defects in the GB region. This is consistent with what is expected when the grain size is not large compared to the depth of the stress distribution [78].

To see the distribution more quantitatively, the stress vs. depth is shown in Fig. 7a for different energies with L=4 nm (the same simulation conditions shown in Fig. 4). For each depth, the stress has been averaged over the lateral x- and y-dimensions of the film. The large tensile stress at the surface is due to the surface stress and is approximately the same for each energy. Directly below the surface, additional tensile stress is generated by the vacancies formed by energetic collisions. As the energy is increased, the depth of this tensile region increases, corresponding to vacancy formation at greater depths. At even deeper depths, the stress becomes compressive; the magnitude and the depth of the compressive region increase with energy, corresponding to the greater number of interstitial defects forming at greater depths.

The average stress in the film is computed by averaging the depth distribution over the film thickness. This is similar to what would be measured in a wafer curvature experiment if the effects of defect diffusivity can be ignored. As shown in Fig. 7b, the average stress increases linearly with the number of energetic Ar particles. The larger slope at higher energy means that there is more stress created per particle.

The stress distribution for different grain sizes after 1200 particles of 100 eV Ar is shown in Fig. 7c. This figure is made from the same set of simulation conditions that are used to produce the defect distributions in Fig. 3. The tensile part of the distribution at the surface is essentially unchanged by the addition of GBs. However, the stress becomes more compressive for small values of L, corresponding to the increased number of interstitials that form at the GB. The average stress vs. the number of incident Ar particles for the different grain sizes is shown in Fig. 7d. The slope is higher for the smaller gain size, indicating that more GBs will absorb more interstitials since GBs can provide more energetically favorable sites, which finally leads to more compressive stress in the

film. In this work we have only looked at one type of GB, but we believe a similar mechanism will operate to generate compressive stress in others.

Fig. 7e shows the stress distribution for L=5 nm in different bombardment directions with an energy of 100 eV. The tensile stress in the surface region shows no significance changes after 1200 collisions in different directions. However, the stress becomes more compressive at the incidence angle of  $20^\circ$ , and the compressive region is also large in the direction, which is related to the defects generated in the region, as shown in Fig. 6. The average stress vs. the number of incident Ar particles for different directions is shown in Fig. 7f. It can be found that the slopes for all directions are less than that in the model of L=4 because of the smaller number of GBs. Similarly, the slopes at different directions have no obvious changes, but at the angle of  $20^\circ$ , it is slightly large, while it is smaller for [111] directions. Such behavior is associated with the many interstitials at the region with depth from 0.5 nm to 2 nm in [001] direction, as well as the implanted Ar atoms.

# 3.4. Relationship of stress and defects

The stress can be related to the defect distribution using a simple model. If we assume that each defect has an average volume associated with it, then the volume of each layer at height *z* changes by:

$$\begin{split} \Delta V(z) &= N_{int}(z)\Omega_{int} + N_{Ar\_int}(z)\Omega_{Ar\_int} + N_{vac}(z)\left(\Omega_{vac} - \Omega_{Mo}\right) \\ &+ N_{Ar\_sub}(z)\left(\Omega_{Ar\_sub} - \Omega_{Mo}\right) \end{split} \tag{1}$$

where  $\Omega_i$  is the relaxed volume of each type of defect (interstitial, vacancy, interstitial Ar or substitutional Ar) or Mo atom, and the relaxed volume of Mo  $(\Omega_{Mo})$  is equal to 0.0156 [79].  $N_i(z)$  is the number of each type of defect; it is the same type of distribution as shown in Fig. 3b except that the number of Ar on interstitial and substitutional sites is separately tracked. Since the film is in a biaxial stress state, the corresponding stress  $\sigma(z)$  in each layer is given by multiplying Eq. (1) by  $-M/(3N_0\Omega_{Mo})$  where M is the biaxial modulus and  $N_o$  is the number of atoms per layer in the simulation.

The stress distribution can, therefore, be written in terms of a linear superposition of the different defect distributions. The coefficients for each term are determined by using least-squares fitting to minimize the difference between the simulated stress distribution and the stress calculated from the defect distribution. Because the equation estimates the stress associated with the presence of defects, it does not account for the surface stress, which is due to broken bonds on the surface. Therefore, the surface stress is removed before fitting by subtracting the relaxed stress distribution before any Ar bombardment from the distribution after bombardment by 1200 Ar particles. A constant offset term is also included in the fitting form to account for potential changes in the surface stress due to surface roughening.

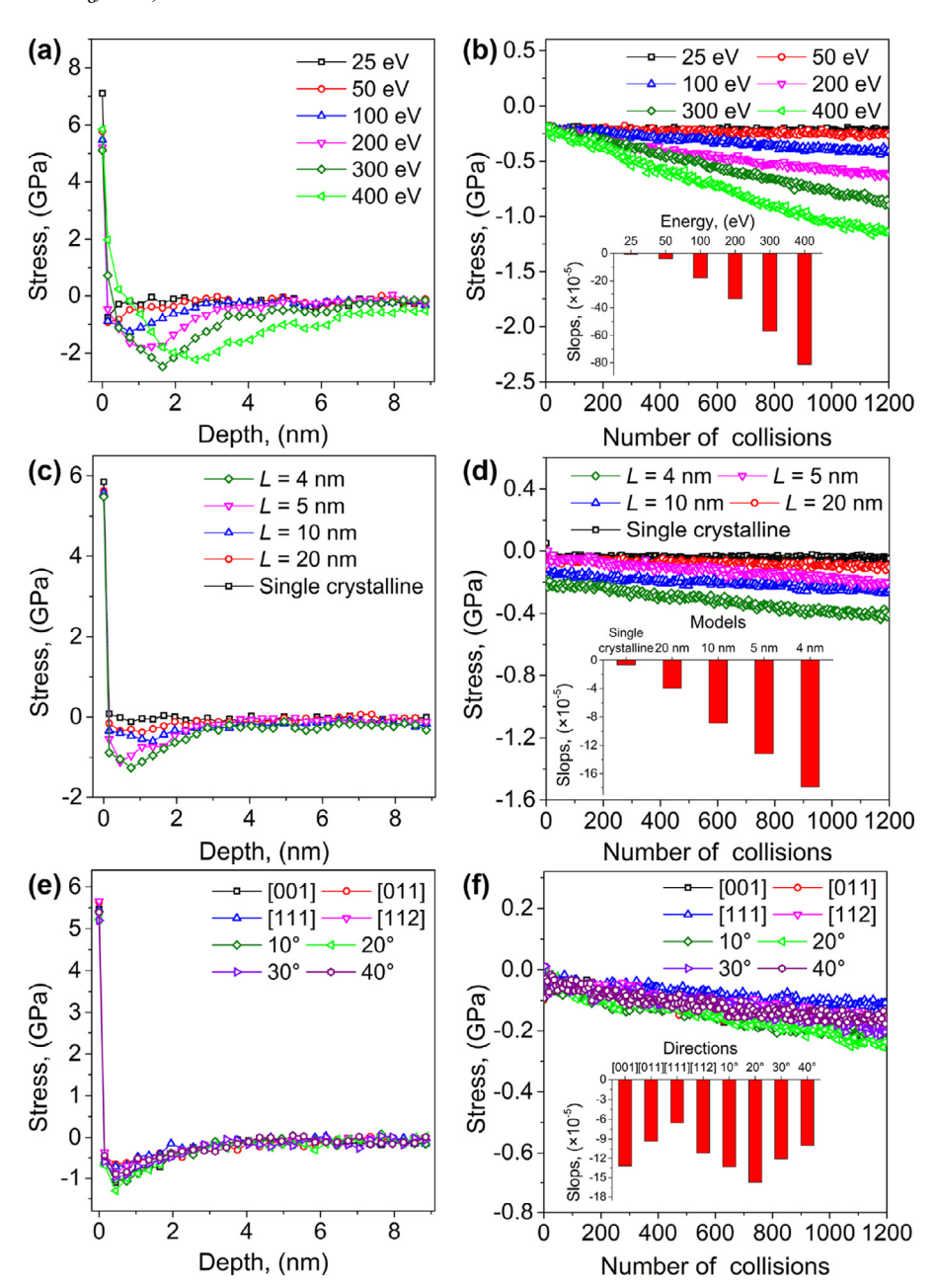


**Fig. 7.** (a) Stress distribution vs. depth for L=4 nm at different Ar energies indicated in figure. (b) Variation of thickness-averaged stress with number of collisions for L=4 nm. (c) Stress distribution vs. depth for 100 eV Ar for different grain sizes indicated in figure. (d) Variation of thickness-averaged stress with number of collisions for 100 eV Ar and different grain sizes. (e) Stress distribution vs. depth for L=5 nm at different incident directions for 100 eV. (f) Variation of thickness-averaged stress with number of collisions for L=5 nm.

Fig. 8 shows the results for different energies at a grain size of L=4 nm. Each stress distribution was fit individually to the corresponding defect distributions to obtain a separate set of coefficients. The fitting form agrees well with the simulated stress which indicates that the point defect distribution is sufficient to characterize the stress induced by energetic particles. Because surface roughness modifies the surface stress, it is difficult to determine its exact contribution to each stress distribution. However, the removal of the initial surface stress after relaxation appears to be an adequate approximation.

Fitting was performed for all the energies and grain sizes simulated in this work. The resulting average values for the relaxation volume of the different defects are shown in Table 3 in units of nm³ and relative to the atomic volume of a Mo atom. The strain around a Mo interstitial is significantly larger than around an Ar interstitial. Generally, the volume values in Mo for different types of interstitial configurations such as <110>, <111> dumbbells and crowdion are in the range (1.02-1.41)  $\Omega_{\rm Mo}$  for different potentials [80], which is slightly smaller than the fitting result in Table 3. The main reason may be that some interstitial

clusters are generated in the bulk at high energy, as can be seen from above discussion regarding the dislocation loops. After calculation, the average  $\Omega_{int}$  at the energies of 50 eV and 100 eV are 1.78  $\Omega_{Mo}$  and 1.46  $\Omega_{Mo}$ , respectively, which are close to the above values. The volume associated with a vacancy is much smaller than a Mo atom, which is attributed to the mechanism of volume change. When a vacancy is formed, the electron redistribution is the major cause of volume change. Therefore, the lattice could be relaxed around a vacancy, even no volume change when a vacancy is formed in the central atom in the regular coordination polyhedron of a FCC lattice [81]. However, for the relaxation volume of interstitials, the major factor is the efficient packing of atoms together with the non-linear elastic deformation [81]. According to the formation volume of the vacancy [79], we find that the  $\Omega_{vac}$  in Mo is about 0.27  $\Omega_{Mo}$  [82] and 0.5  $\Omega_{Mo}$  [83] calculated by using atomic simulation and first-principles calculations, respectively. Thus, the values in Table 3 are in good agreement with the previous studies. The volume of Ar in a substitutional site is also much smaller than a Mo atom. Similar fitting was also performed in which the separate distributions of

**Table 3**Defect volume estimated from fitting the stress to a superposition of defect distributions (top row) and from relaxation of the lattice around inserted defects (bottom row).

Defect volume (nm <sup>3</sup> )	$\Omega_{\mathrm{int}}$	$\Omega_{ m vac}$	$\Omega_{\text{Ar\_int}}$	$\Omega_{\text{Ar\_sub}}$
From fitting defect	0.030 +/- 0.01	0.0036 +/- 0.0081	0.0014 +/- 0.023	0.011 +/- 0.090
distributions Relaxation around	(1.92 Ω <sub>Mo</sub> ) 0.019 +/- 0.001	$(0.23  \Omega_{Mo}) \ 0.0071  +/-  0.001$	$(0.093 \ \Omega_{Mo})$ 0.0017 +/- 0.0004	(0.70 Ω <sub>Mo</sub> ) 0.012 +/- 0.001
inserted defects	$(1.22 \Omega_{Mo})$	$(0.45 \Omega_{Mo})$	$(0.11 \ \Omega_{Mo})$	$(0.77 \Omega_{Mo})$

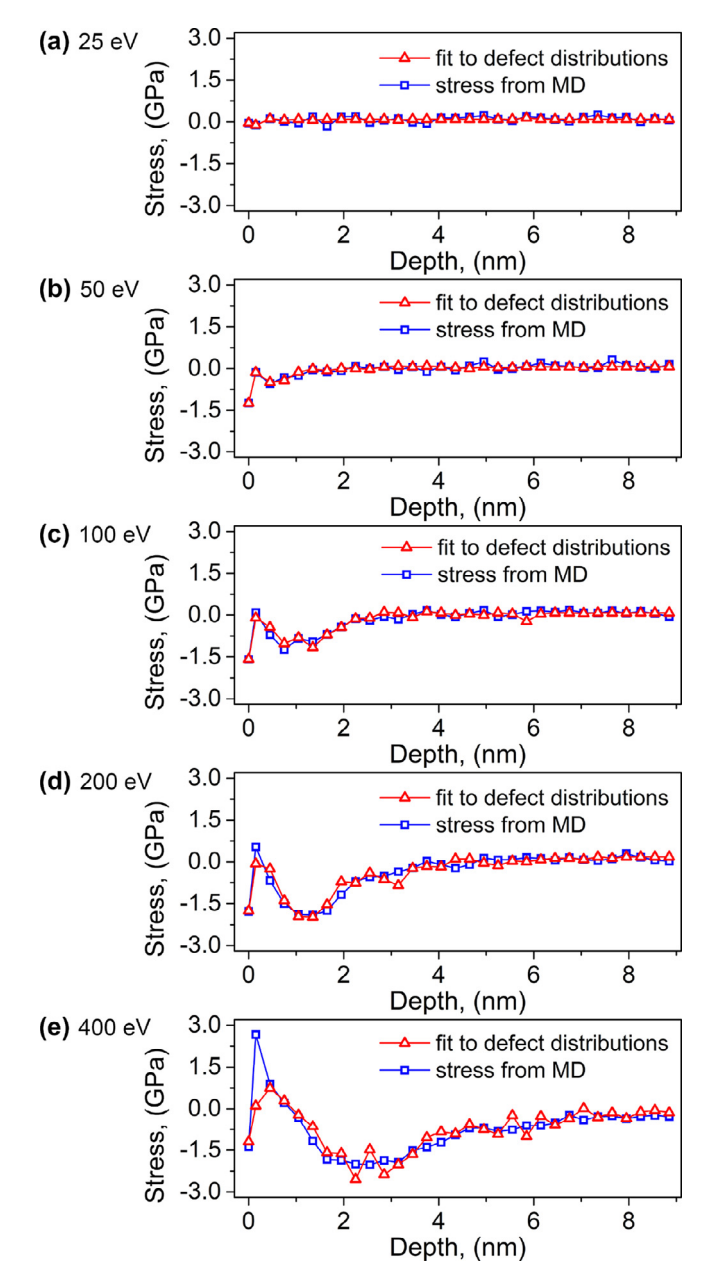


**Fig. 8.** Compare stress distribution with fit from defect distributions for L=4 nm model at different energies: (a) 25 eV, (b) 50 eV, (c) 100 eV, (d) 200 eV, and (e) 400 eV.

Mo interstitials in the bulk and at the GB were considered. The results (not shown) are similar to those discussed here, but the large error bars on the fitting parameters make it impossible to make any conclusions about the relative sizes of the two types of interstitials.

For comparison, the relaxation volume was also computed by inserting a random distribution of defects of each type into a simulated film

with no GBs. The model was then relaxed, and the corresponding stress was calculated. The relaxed volume around each type of defect calculated by this method is shown in the bottom row of Table 3. The results are similar, though the volume around the Mo interstitial is smaller, and the vacancy larger than obtained from the fitting.

The fact that the stress induced by particle bombardment can be modeled by the defect distribution is extremely useful for future modeling studies. To consider the larger time scale associated with diffusional kinetics, it is necessary to consider other simulation schemes such as kinetic Monte Carlo (kMC). The results here show that the stress can be estimated from the defect distribution, which supports assumptions made in prior work that we have performed to incorporate stress into kMC by counting the interstitial defects incorporated into the GB during non-energetic growth [84].

#### 3.5. Significance for processing

The simulation results indicate that the stress becomes more compressive when there are GBs. The GB enhancement is even greater at higher energies. This effect means that smaller grain materials will develop more compressive stress with energetic bombardment. GBs are not included in many models that focus on point defect generation or average energy deposition, but it is consistent with the GB-based mechanisms used to model stress in sputter-deposited films [17]. Although only one type of GB was studied in this work, it is expected that the mechanism of stabilizing interstitial defects will hold for other GB structures.

The results described above are for a bombardment of a static surface, not for thin-film growth. Instead of the near-surface region getting more compressive with time, a growing film will develop a steady-state stress as previously-implanted defects get buried beneath the growing surface. If the relaxation of the film due to defect dynamics is ignored, the steady-state stress can be estimated from the stress distribution produced by the MD simulations:

$$\sigma_{ss} = \int \sigma_{defect}(z) dz \left( \frac{400 \ nm^2}{1200 \ particles} \right) \frac{\phi_{energ}}{R} \tag{2}$$

where  $\sigma_{defect}(z)$  is the stress from the defects (i.e., with the surface stress removed) and the factor (400/1200) is used to scale the stress by the Ar fluence used in the simulation.  $\phi_{energ}$  is the flux of energetic particles, and R is the growth rate. R can also be expressed as  $\phi_{dep}/\rho_{dep}$  where  $\phi_{dep}$  is the flux of the deposited (film) atoms and  $\rho_{dep}$  is the density of the film. Written this way, the steady-state stress can be seen to depend on the ratio of energetic particles to deposited film atoms ( $\phi_{energ}/\phi_{dep}$ ), i.e., on the number of energetic particles arriving per layer. If there are multiple species of energetic particles as in sputter deposition (e.g., inert Ar atoms and energetic deposited species), the stress distribution in Eq. (2) can be replaced by a superposition of stresses from each species multiplied by the corresponding flux.

To compare the predictions of the MD simulations with experiments [38], we use Eq. (2) to estimate the steady-state stress during sputter deposition of Mo. A combination of SIMTRA [85] and SRIM [48] calculations was performed in order to estimate the energy and fluxes of the species needed for this calculation. For an Ar pressure of 0.11 Pa, the average energy of both the Ar and Mo species was 23.7 eV, and the ratio of the Ar:Mo flux was 0.18. Therefore, MD simulations were performed

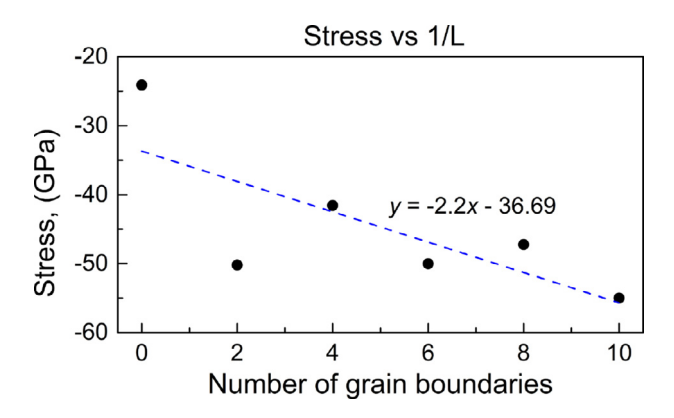


Fig. 9. Plot of the steady-state stress of 25 eV Ar/Mo sputtering, calculated for different numbers of GBs.

using 25 eV Ar and Mo bombardment on Mo in order to get the stress distribution generated by each species at the different grain sizes considered above. The results for Ar and Mo bombardment were combined with appropriate weighting for their relative fluxes to estimate the total stress distribution generated during film deposition.

A plot of the steady-state stress calculated for different numbers of GBs (proportional to 1/L) is shown in Fig. 9. The figure indicates that the magnitude of the compressive stress increases roughly linearly with the number of GBs. It is independent of the growth rate because SIMTRA assumes that the ratio of the fluxes of energetic Ar to Mo remains the same for different deposition rates. The deviation of the results from a linear dependence may be attributed to statistical variations in the individual simulations, as well as to potential error associated with the removal of the surface stress.

Evaluating the linear fit at the grain size used in the experiments (50 nm) produces an estimate for the steady-state stress of -35.1 GPa. This value is much larger than would be seen in an experiment because the calculation ignores any post-impact relaxation of the stress by diffusion-mediated annihilation of the defects. The separate contributions of energetic bombardment in the bulk of the film and at the GBs can be determined by further consideration of Fig. 9. The value of the linear fit for no GBs (-36.69 GPa) is due solely to stress generation in the bulk. The slope of the line (-2.2 GPa per GB) is the amount of additional stress generated per GB minus the small amount of bulk film that is removed by adding GBs.

The division of the stress generation into bulk and GB terms is also an integral part of the analytical model that has been proposed to explain stress in sputtered films [17], where they are referred to as  $\sigma_{bulk}^{energetic}$  and  $\sigma^{\textit{energetic}}_{\textit{i}}$  , respectively. In this paper, measurements of stress in sputtered Mo were fit to this model to produce a set of parameters for the stress produced by energetic particles. The GB term  $\sigma_{ab}^{energetic}$  attributes the stress to diffusion-less addition of atoms into it, which is similar to what is seen in the MD simulations. From fitting to the analytical model, the grain-size dependent contribution to the stress is predicted to be -2.9 GPa per GB, which compares favorably with the slope in Fig. 9 of -2.2 GPa per GB. The bulk term  $\sigma_{bulk}^{energetic}$  describes the stress due to the generation of point defects in the film. Fitting the data predicts a stress of -44.7 GPa if relaxation by the diffusion of defects is ignored. In comparison, the linear fit in Fig. 9 predicts the value of-36.7 GPa. If defect diffusion is not ignored, the model for  $\sigma_{bulk}^{energetic}$  also includes a factor to account for relaxation of the stress by diffusion of these defects to the surface. Using the parameters from the fitting, defect diffusion and annihilations are predicted to reduce the bulk stress by a factor of 0.0142 at a growth rate of 0.1 nm/s. Therefore, when diffusion is included, the contribution of point defects in the bulk to the compressive stress is reduced to -0.64 GPa, which is similar to values seen in the measurements. The similarity in the results obtained from the MD simulations and the analytical model suggests that the mechanisms used in the model are physically reasonable. This provides support for the use of the model to interpret stress during sputter deposition.

MD is a difficult and relatively time-consuming technique, so other ways of estimating the defect distribution would be useful. A commonly-used alternative method for modeling defects created by energetic particles is the SRIM program [48], based on a binary collision approximation. We, therefore, performed simulations with SRIM to compare its predictions with the work discussed here. In general, we found that SRIM underestimates the depth of the defect production at the energies considered in this work. One reason for this is that SRIM does not consider crystallographic effects. Channeling of the energetic particles by atoms on the lattice means that the range of implanted Ar simulated by MD is significantly larger than predicted by SRIM. In addition, the presence of GBs is not included in SRIM. As seen above, these greatly increase the number and depth of interstitial defects produced by energetic particles. So although SRIM can provide useful guidance, it is not an adequate substitute for MD.

#### 4. Conclusions

The generation and evolution of defects in polycrystalline Mo films caused by energetic Ar atoms and their effect on stress evolution are simulated using MD. The results show that GBs play an important role in the defect and stress generation. A mechanism of sequential collisions is observed that enables atoms to be displaced from the lattice far from the site of the initial impact. The GBs act as sinks that stabilize the displaced atoms, and a larger number of interstitials are produced at a larger depth at GBs than elsewhere. The effect becomes more significant at larger energy and smaller grain size. For other defects, the effect of GBs on their production is small.

The stress distributions from the MD simulations can be explained in terms of the strain generated around particle-induced defects. By fitting the distribution to a superposition of defect distributions, estimates for the relaxation volume of the different defects are produced. The residual stress in a sputter-deposited thin film is estimated by assuming that there is no relaxation by diffusion of the defects. The contributions of bulk and GB effects to the total stress were determined by comparing the results of simulations with different grain sizes. The resulting steady-state stress values are consistent with measurements of sputtered Mo films and the parameters determined from fitting the data to a rate equation-based model of stress in sputtered films.

The small accessible time scale of MD makes it difficult to directly extend the current work to include defect dynamics or film growth. However, the recognition that the defect distribution can act as a proxy for the stress means that it can be modeled without having to calculate the stress directly. The bombardment-induced defect distribution calculated by MD can be used to inform other kinds of simulations, e.g., kMC simulations [86] or rate equations [39, 43]. This enables the stress-inducing effects of energetic particles to be combined with defect diffusion and a deposition flux. This type of modeling will be performed in the future.

# **Declaration of Competing Interest**

None.

# Acknowledgments

This work was supported by the National Science Foundation (NSF) under Contracts No. DMR-1602491 and DMR-2006422, the National Science Foundation of China under Contract No. 52075417, and the Scholarship of China Scholarship Council.

## Supplementary materials

Supplementary material associated with this article can be found, in the online version, at doi:10.1016/j.mtla.2021.101043.

#### References

- R. Roy, Low-energy ion-assisted deposition of metal-films, Surf. Coat. Technol. 51 (1-3) (1992) 203–211.
- [2] J.A. Thornton, D.W. Hoffman, Stress-related effects in thin-films, Thin Solid Films 171 (1) (1989) 5–31.
- [3] T.G. Bifano, H.T. Johnson, P. Bierden, R.K. Mali, Elimination of stress-induced curvature in thin-film structures, J. Microelectromech. Syst. 11 (5) (2002) 592–597.
- [4] F.M. Dheurle, J.M.E. Harper, Note on the origin of intrinsic stresses in films deposited via evaporation and sputtering, Thin Solid Films 171 (1) (1989) 81–92.
- [5] F.M. Dheurle, Aluminum films deposited by rf sputtering, Metall. Trans. 1 (3) (1970) 725 &.
- [6] K.H. Muller, Ion-beam-induced epitaxial vapor-phase growth a molecular-dynamics study. Phys. Rev. B, 35 (15) (1987) 7906–7913.
- [7] H. Windischmann, An intrinsic stress scaling law for polycrystalline thin-films prepared by ion-beam sputtering, J. Appl. Phys. 62 (5) (1987) 1800–1807.
- [8] O. Knotek, R. Elsing, G. Kramer, F. Jungblut, On the origin of compressive stress in pvd coatings - an explicative model, Surf. Coat. Technol. 46 (3) (1991) 265–274.
- [9] H. Windischmann, Intrinsic stress in sputtered thin-films, J. Vac. Sci. Technol. Vac. Surf. Films 9 (4) (1991) 2431–2436.
- [10] C.A. Davis, A simple-model for the formation of compressive stress in thin-films by ion-bombardment, Thin Solid Films 226 (1) (1993) 30–34.
- [11] Y.V. Martynenko, G. Carter, Stress evolution in ion-assisted thin metal-film deposition, Radiat. Eff. Defect Solids 132 (2) (1994) 103–118.
- [12] J.D. Kamminga, T.H. de Keijser, R. Delhez, E.J. Mittemeijer, On the origin of stress in magnetron sputtered tin layers, J. Appl. Phys. 88 (11) (2000) 6332–6345.
- [13] Y. Pauleau, Generation and evolution of residual stresses in physical vapour-deposited thin films, Vacuum 61 (2-4) (2001) 175–181.
- [14] G. Knuyt, A model for the behaviour of tensile and compressive residual stresses developed in thin films produced by ion beam-assisted deposition techniques, Thin Solid Films 467 (1-2) (2004) 275–283.
- [15] L.E. Koutsokeras, G. Abadias, Intrinsic stress in zrn thin films: evaluation of grain boundary contribution from in situ wafer curvature and ex situ x-ray diffraction techniques, J. Appl. Phys. 111 (9) (2012) 093509.
- [16] D. Magnfalt, G. Abadias, K. Sarakinos, Atom insertion into grain boundaries and stress generation in physically vapor deposited films, Appl. Phys. Lett. 103 (5) (2013) 051910.
- [17] E. Chason, M. Karlson, J.J. Colin, D. Magnfalt, K. Sarakinos, G. Abadias, A kinetic model for stress generation in thin films grown from energetic vapor fluxes, J. Appl. Phys. 119 (14) (2016) 145307.
- [18] M. Samaras, P.M. Derlet, H. Van Swygenhoven, M. Victoria, Atomic scale modelling of the primary damage state of irradiated fcc and bcc nanocrystalline metals, J. Nucl. Mater. 351 (1-3) (2006) 47–55.
- [19] W.Z. Han, M.J. Demkowicz, E.G. Fu, Y.Q. Wang, A. Misra, Effect of grain boundary character on sink efficiency, Acta Mater. 60 (18) (2012) 6341–6351.
- [20] A. Esfandiarpour, S.A.H. Feghhi, A.A. Shokri, Effects of atomic grain boundary structures on primary radiation damage in alpha-Fe, Nucl. Instrum. Method B 362 (2015) 1–8.
- [21] M. Samaras, P.M. Derlet, H. Van Swygenhoven, M. Victoria, Stacking fault tetrahedra formation in the neighbourhood of grain boundaries, Nucl. Instrum. Method B 202 (2003) 51–55
- [22] K.Y. Yu, D. Bufford, F. Khatkhatay, H. Wang, M.A. Kirk, X. Zhang, In situ studies of irradiation-induced twin boundary migration in nanotwinned Ag, Scr. Mater. 69 (5) (2013) 385–388.
- [23] N. Li, J. Wang, Y.Q. Wang, Y. Serruys, M. Nastasi, A. Misra, Incoherent twin boundary migration induced by ion irradiation in Cu, J. Appl. Phys. 113 (2) (2013).
- [24] B. Li, X.J. Long, Z.W. Shen, S.N. Luo, Interactions between displacement cascades and Sigma 3 < 110 > tilt grain boundaries in Cu, J. Nucl. Mater. 481 (2016) 46–52.
- [25] X.Y. Wang, N. Gao, W. Setyawan, B. Xu, W. Liu, Z.G. Wang, Effect of irradiation on mechanical properties of symmetrical grain boundaries investigated by atomic simulations, J. Nucl. Mater. 491 (2017) 154–161.
- [26] P. Sigmund, R.In Behrisch, in: Sputtering by Particle Bombardment, Springer, Berlin, 1981 p. 49
- [27] J.A. Thornton, J. Tabock, D.W. Hoffman, Internal-stresses in metallic-films deposited by cylindrical magnetron sputtering, Thin Solid Films 64 (1) (1979) 111–119.
- [28] A. Debelle, G. Abadias, A. Michel, C. Jaouen, V. Pelosin, Growth stress buildup in ion beam sputtered mo thin films and comparative study of stress relaxation upon thermal annealing or ion irradiation, J. Vac. Sci. Technol. A 25 (5) (2007) 1438–1448.
- [29] T.D. delaRubia, Irradiation-induced defect production in elemental metals and semiconductors: a review of recent molecular dynamics studies, Annu. Rev. Mater. Sci. 26 (1996) 613–649.
- [30] K. Nordlund, M. Ghaly, R.S. Averback, M. Caturla, T.D. de la Rubia, J. Tarus, Defect production in collision cascades in elemental semiconductors and fcc metals, Phys. Rev. B 57 (13) (1998) 7556–7570.
- [31] C.M. Gilmore, J.A. Sprague, Molecular-dynamics simulation of the energetic deposition of ag thin-films, Phys. Rev. B 44 (16) (1991) 8950–8957.
- [32] S.P. Kim, H.B. Chew, E. Chason, V.B. Shenoy, K.S. Kim, Nanoscale mechanisms of surface stress and morphology evolution in FCC metals under noble-gas ion bombardments, Proc. R. Soc. Math. Phy. 468 (2145) (2012) 2550–2573.
- [33] N.A. Marks, D.R. McKenzie, B.A. Pailthorpe, Molecular-dynamics study of compressive stress generation, Phys. Rev. B 53 (7) (1996) 4117–4124.
- [34] R.W. Smith, D.J. Srolovitz, Void formation during film growth: A molecular dynamics simulation study, J. Appl. Phys. 79 (3) (1996) 1448–1457.
- [35] X.W. Zhou, R.A. Johnson, H.N.G. Wadley, A molecular dynamics study of nickel vapor deposition: temperature, incident angle, and adatom energy effects, Acta Mater. 45 (4) (1997) 1513–1524.

- [36] X.Y. Zhou, X.X. Yu, D. Jacobson, G.B. Thompson, A molecular dynamics study on stress generation during thin film growth, Appl. Surf. Sci. 469 (2019) 537–552.
- [37] X.W. Zhou, H.N.G. Wadley, Hyperthermal vapor deposition of copper: athermal and biased diffusion effects, Surf. Sci. 431 (1-3) (1999) 42–57.
- [38] A. Fillon, G. Abadias, A. Michel, C. Jaouen, Stress and microstructure evolution during growth of magnetron-sputtered low-mobility metal films: Influence of the nucleation conditions, Thin Solid Films 519 (5) (2010) 1655–1661.
- [39] Y. Ishii, C.S. Madi, M.J. Aziz, E. Chason, Stress evolution in Si during low-energy ion bombardment, J. Mater. Res. 29 (24) (2014) 2942–2948.
- [40] H.C. Huang, G.H. Gilmer, T.D. de la Rubia, An atomistic simulator for thin film deposition in three dimensions, J. Appl. Phys. 84 (7) (1998) 3636–3649.
- [41] Y.G. Yang, X.W. Zhou, R.A. Johnson, H.N.G. Wadley, Monte Carlo simulation of hyperthermal physical vapor deposition, Acta Mater. 49 (16) (2001) 3321–3332.
- [42] I. Martin-Bragado, A. Rivera, G. Valles, J.L. Gomez-Selles, M.J. Caturla, Mmonca: an object kinetic monte carlo simulator for damage irradiation evolution and defect diffusion, Comput. Phys. Commun. 184 (12) (2013) 2703–2710.
- [43] W.L. Chan, E. Chason, Stress evolution and defect diffusion in cu during low energy ion irradiation: experiments and modeling, J. Vac. Sci. Technol. A 26 (1) (2008) 44–51.
- [44] K. Morita, H. Nakashima, Atomic periodicity of <001>symmetric tilt boundary in molybdenum, Mater. Sci. Eng. Struct. 234 (1997) 1053–1056.
- [45] X.Y. Li, W. Liu, Y.C. Xu, C.S. Liu, Q.F. Fang, B.C. Pan, J.L. Chen, G.N. Luo, Z.G. Wang, Principal physical parameters characterizing the interactions between irradiation-induced point defects and several tilt symmetric grain boundaries in Fe, Mo and W, J. Nucl. Mater. 444 (1-3) (2014) 229–236.
- [46] S. Plimpton, Computational limits of classical molecular-dynamics simulations, Comp Mater. Sci. 4 (4) (1995) 361–364.
- [47] C.K. Kim, A. Kubota, D.J. Economou, Molecular dynamics simulation of silicon surface smoothing by low-energy argon cluster impact, J. Appl. Phys. 86 (12) (1999) 6758–6762.
- [48] J.F. Ziegler, M.D. Ziegler, J.P. Biersack, SRIM The stopping and range of ions in matter (2010), Nucl. Instrum. Methods B 268 (11-12) (2010) 1818–1823.
- [49] G.J. Ackland, R. Thetford, An improved n-body semiempirical model for body-centered cubic transition-metals, Philos. Mag. A 56 (1) (1987) 15–30.
- [50] A. Rytkonen, S. Valkealahti, M. Manninen, Melting and evaporation of argon clusters, J. Chem. Phys. 106 (5) (1997) 1888–1892.
- [51] K.K. Kammara, R. Kumar, F.S. Donbosco, Reconsideration of metal surface sputtering due to bombardment of high-energy argon ion particles: a molecular dynamics study, Comput. Part. Mech. 3 (1) (2016) 3–13.
- [52] K. Gartner, D. Stock, B. Weber, G. Betz, M. Hautala, G. Hobler, M. Hou, S. Sarite, W. Eckstein, J.J. Jimenezrodriguez, A.M.C. Perezmartin, E.P. Andribet, V. Konoplev, A. Grasmarti, M. Posselt, M.H. Shapiro, T.A. Tombrello, H.M. Urbassek, H. Hensel, Y. Yamamura, W. Takeuchi, Round-robin computer-simulation of ion transmission through crystalline layers, Nucl. Instrum. Methods B 102 (1-4) (1995) 183–197.
- [53] M. Tikhonchev, V. Svetukhin, A. Kadochkin, E. Gaganidze, MD simulation of atomic displacement cascades in Fe-10 at. %Cr binary alloy, J. Nucl. Mater. 395 (1-3) (2009) 50-57
- [54] A. Stukowski, Visualization and analysis of atomistic simulation data with OVI-TO-the open visualization tool, Model. Simul. Mater. Sci 18 (1) (2010) 015012.
- [55] A. Stukowski, K. Albe, Dislocation detection algorithm for atomistic simulations, Model. Simul. Mater. Sci. 18 (2) (2010).
- [56] E. Wigner, F. Seitz, On the constitution of metallic sodium, Phys. Rev. 43 (10) (1933) 0804–0810.
- [57] G. Voronoi, Nouvelles applications des paramètres continus à la théorie des formes quadratiques, J. Reine Angew. Math. 134 (1908) 198–287.
- [58] D.M. Heyes, Pressure tensor of partial-charge and point-dipole lattices with bulk and surface geometries, Phys. Rev. B 49 (2) (1994) 755–764.
- [59] A.P. Thompson, S.J. Plimpton, W. Mattson, General formulation of pressure and stress tensor for arbitrary many-body interaction potentials under periodic boundary conditions, J. Chem. Phys. 131 (15) (2009) 154107.
- [60] K. Nordlund, S.J. Zinkle, A.E. Sand, F. Granberg, R.S. Averback, R.E. Stoller, T. Suzudo, L. Malerba, F. Banhart, W.J. Weber, F. Willaime, S.L. Dudarev, D. Simeone, Primary radiation damage: a review of current understanding and models, J. Nucl. Mater. 512 (2018) 450–479.
- [61] W. Zag, K. Urban, Temperature-dependence of the threshold energy for atom displacement in irradiated molybdenum, Phys. Status Solidi Appl. Res. 76 (1) (1983) 285–295.
- [62] F. Maury, P. Vajda, M. Biget, A. Lucasson, P. Lucasson, Anisotropy of the displacement energy in single crystals of molybdenum, Radiat. Eff Defect S 25 (3) (1975) 175–185.
- [63] J. Loffler, J. Weissmuller, Grain-Boundary Atomic-structure in nanocrystalline palladium from X-ray atomic distribution-functions, Phys. Rev. B 52 (10) (1995) 7076–7093.
- [64] E.A. Stern, R.W. Siegel, M. Newville, P.G. Sanders, D. Haskel, Are nanophase grain-boundaries anomalous, Phys. Rev. Lett. 75 (21) (1995) 3874–3877.
- [65] P. Keblinski, D. Wolf, S.R. Phillpot, H. Gleiter, Structure of grain boundaries in nanocrystalline palladium by molecular dynamics simulation, Scr. Mater. 41 (6) (1999) 631–636.
- [66] H. Van Swygenhoven, D. Farkas, A. Caro, Grain-boundary structures in polycrystalline metals at the nanoscale, Phys. Rev. B 62 (2) (2000) 831–838.
- [67] M. Samaras, P.M. Derlet, H. Van Swygenhoven, M. Victoria, Computer simulation of displacement cascades in nanocrystalline Ni, Phys. Rev. Lett. 88 (12) (2002) 125505.
- [68] T.D. Shen, Radiation tolerance in a nanostructure: is smaller better? Nucl. Instrum. Method B 266 (6) (2008) 921–925.
- [69] R.H. Silsbee, Focusing in collision problems in solids, J. Appl. Phys. 28 (11) (1957) 1246–1250.

- [70] S.V. Starikov, Z. Insepov, J. Rest, A.Y. Kuksin, G.E. Norman, V.V. Stegailov, A.V. Yanilkin, Radiation-induced damage and evolution of defects in Mo, Phys. Rev. B 84 (10) (2011).
- [71] C.A. English, M.L. Jenkins, Molecular ion irradiations of molybdenum, Philos. Mag. 90 (7-8) (2010) 821–843.
- [72] J. Bohdansky, A universal relation for the sputtering yield of monatomic solids at normal ion incidence, Nucl. Instrum. Methods B 2 (1-3) (1984) 587–591.
- [73] P. Sigmund, Theory of sputtering i. sputtering yield of amorphous and polycrystalline targets, Phys. Rev. 184 (2) (1969) 383 +.
- [74] S.M. Wu, R. van de Kruijs, E. Zoethout, F. Bijkerk, Sputtering yields of Ru, Mo, and Si under low energy Ar+ bombardment, J. Appl. Phys. 106 (5) (2009).
- [75] B. Czerwinski, L. Rzeznik, R. Paruch, B.J. Garrison, Z. Postawa, Effect of impact angle and projectile size on sputtering efficiency of solid benzene investigated by molecular dynamics simulations, Nucl. Instrum. Methods B 269 (14) (2011) 1578–1581.
- [76] K. Harafuji, K. Kawamura, Sputtering yield as a function of incident ion energy and angle in wurtzite-type GaN crystal, Jpn. J. Appl. Phys. 47 (3) (2008) 1536–1540.
- [77] R.C. Cammarata, Surface and interface stress effects in thin-films, Prog. Surf. Sci. 46 (1) (1994) 1–38.
- [78] E. Chason, P.R. Guduru, Tutorial: understanding residual stress in polycrystalline thin films through real-time measurements and physical models, J. Appl. Phys. 119 (19) (2016) 191101.

- [79] O.Le Bacq, F. Willaime, A. Pasturel, Unrelaxed vacancy formation energies in group-iv elements calculated by the full-potential linear muffin-tin orbital method: invariance with crystal structure, Phys. Rev. B 59 (13) (1999) 8508–8515.
- [80] G. Simonelli, R. Pasianot, E.J. Savino, Self-interstitial configuration in bcc metals. an analysis based on many-body potentials for fe and mo, Phys. Status Solidi B 217 (2) (2000) 747–758.
- [81] W.G. Wolfer, A novel-approach to compute the relaxation volume of self-interstitials in metals, J. Phys. F Met. Phys. 12 (3) (1982) 425–433.
- [82] J.M. Harder, D.J. Bacon, Point-defect and stacking-fault properties in body-centered-cubic metals with n-body interatomic potentials, Philos. Mag. A 54 (5) (1986) 651–661.
- [83] P. Soderlind, L.H. Yang, J.A. Moriarty, J.M. Wills, First-principles formation energies of monovacancies in bcc transition metals, Phys. Rev. B 61 (4) (2000) 2579–2586.
- [84] E. Chason, A.F. Bower, Kinetic monte carlo simulations of stress and morphology evolution in polycrystalline thin films, J. Appl. Phys. 125 (11) (2019) 115304.
- [85] K. Van Aeken, S. Mahieu, D. Depla, The metal flux from a rotating cylindrical magnetron: a monte carlo simulation, J. Phys. D Appl. Phys. 41 (20) (2008) 205307.
- [86] H.N.G. Wadley, A.X. Zhou, R.A. Johnson, M. Neurock, Mechanisms, models and methods of vapor deposition, Prog. Mater. Sci. 46 (3-4) (2001) 329–377.